applied optics

Biosensors based on Bloch surface waves in one-dimensional photonic crystal with graphene nanolayers

H. Kaviani Baghbadorani, J. Barvestani,* and S. Roshan Entezar

Faculty of Physics, University of Tabriz, Tabriz, Iran
**Corresponding author: barvestani@tabrizu.ac.ir*

Received 6 September 2016; revised 13 December 2016; accepted 13 December 2016; posted 14 December 2016 (Doc. ID 275281); published 12 January 2017

In biosensors research, much effort has been made to achieve high sensitivity to detect lower concentrations of analyte in a solution by testing different kinds of materials. In this paper, we present a biosensor based on Bloch surface waves made of photonic crystal (PhC) including graphene nanolayers under the Kretschmann configuration. The band structures, surface modes, reflectivity, and sensitivity of the PhC biosensor are calculated by the transfer matrix method and results are compared with those of the structure without graphene layers. Our investigations show that the angular sensitivity of the biosensor considerably increases in the presence of the graphene layers. Moreover, we study the effect of the number of the graphene layers placed on the surface of the biosensor on the performance of our proposed biosensor. The results reveal that the sensitivity of the biosensor is enhanced by increasing the number of graphene layers on the surface due to the π-stacking interactions between graphene's honeycomb cells and the carbon rings in biomolecules. Furthermore, our results show that the phase sensitivity is higher than the angular sensitivity, which can promote the accuracy of the calculations.

OCIS codes: (050.5298) Photonic crystals; (280.4788) Optical sensing and sensors; (240.6690) Surface waves; (240.6680) Surface plasmons.

https://doi.org/10.1364/AO.56.000462

1. INTRODUCTION

In the past two decades, photonic crystals (PhCs) have attracted a great deal of interest in the field of electronics and photonics [1,2]. They have specific properties to prohibit electromagnetic (EM) waves from propagating in certain frequencies (forbidden bands or stopbands) or to guide them in particular directions (passband) [3,4]. Investigations have shown that these infinite periodic layered media or photonic bandgap (PBG) materials are able to support Bloch surface waves (BSWs) or Tamm states when they are truncated [5,6]. The BSWs are electromagnetic waves localized at the interface between a homogeneous and a periodic dielectric media [7], two PhCs [8], or a PhC and a left-handed metamaterial [9], and they decay exponentially along the normal direction away from the surface into both media [10]. Surface modes, particularly the BSWs, are valuable tools for studying surface interactions and sensing [11,12]. To date, numerous studies have experimentally and theoretically demonstrated the superiority of sensors based on BSWs over sensors based on surface plasmon (SP) waves, which are collective oscillations of charge density at the interface between a metal and a dielectric layer [13–21]. Because of the low losses and flexibility in designing PBG materials, the BSW sensors have higher surface sensitivity than SP sensors [22]. The Kretschmann configuration is a great technique for exciting surface waves (SWs) [16,23–26]. In this configuration, by using an appropriate prism, light is coupled to the non-radiative SW. The excitation of SWs can be realized by a dip appearing in the reflection spectrum. The dip location depends on the refractive index of biomolecules that are immobilized at the interface between the sensor and the fluid in which an analyte exists [24–27]. In the investigation of the performance of an optical biosensor, several parameters have great importance: (1) the depth and the width of the dip in the reflectance spectrum [14], (2) the limit of detection [28], (3) the sensitivity [14,22], etc. The sensitivity of the biosensor is one of the most valuable parameters to evaluate biosensor performance and is defined as a response to the variation of the output signal (physical/chemical variation) caused by the target analyte in the surface [28]. Many efforts have been made to enhance the optical sensor's sensitivity by testing different kinds of materials to improve the sensor's performance. Recently, graphene, a real two-dimensional crystal of carbon atoms arranged in a honeycomb lattice that has attracted considerable scientific

interest, has shown great potential in a variety of applications in optoelectronics and plasmonics, such as field-effect transistors, photovoltaic devices, and biosensors [29–31]. Graphene is a gapless semiconductor with very high electron mobility whose transport characteristics and optical conductivity (σ_g) can be tuned by either electrostatic or magneto-static gating or chemical doping [32,33]. In this paper, a model of one-dimensional photonic crystal (1D-PhC) biosensors that include graphene sheets under the Kretschmann configuration in TM polarization is developed by the transfer matrix method (Section 2). In Section 3, we shall study the influence of graphene layers on the performance of our proposed structure and compare it with a conventional PhC biosensor. Finally, conclusions are given in Section 4.

2. THEORETICAL MODEL

In our study, a PhC structure under the well-known Kretschmann configuration is proposed. It consists of a repeating multilayer of two nonmagnetic dielectric materials A and B and graphene nanolayers embedded between two adjacent layers with the permittivities of ε_a and ε_b and thicknesses of d_a and d_b, respectively (Fig. 1). The PhC is capped by a layer of the same material A, but with different width, $d_c = d_t + d_s$. A prism with refractive index $n_p = 1.515$ (BK7) is included at the entrance side of the proposed biosensor. The exit side of the biosensor may contain some graphene layers, which we call surface graphene layers.

To calculate the dispersion relation of BSWs, the reflection, and the sensitivity of the biosensor, we used the well-known transfer matrix method [34]. The electromagnetic fields of the TM polarized wave ($H_x = H_z = 0, E_x = 0$) in each layer (j) can be written

$$\begin{cases} H_{yj}(x,z,t) = H_{yj}(z)\exp\, i(k\beta x - \omega t) \\ E_{xj}(x,z,t) = E_{xj}(z)\exp\, i(k\beta x - \omega t)), \\ E_{zj}(x,z,t) = E_{zj}(z)\exp\, i(k\beta x - \omega t) \end{cases} \tag{1}$$

where $k = \omega/c$ is the vacuum wave number, and $\beta = n_p \sin\theta_0$ is the normalized wave number along the interface.

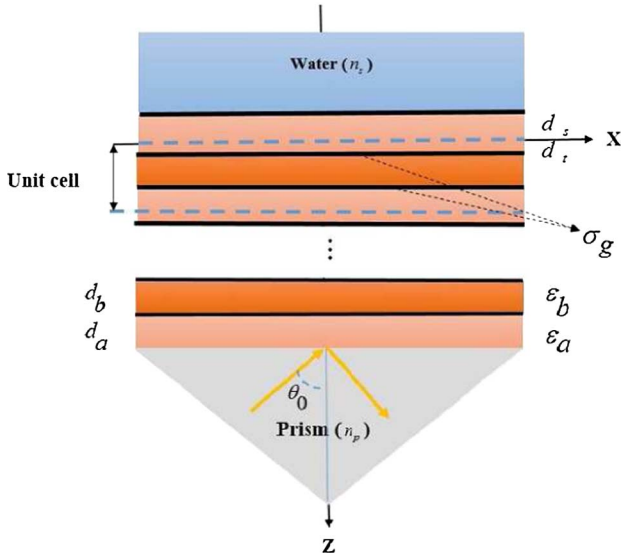

Fig. 1. Schematic representation of the biosensor.

Here the amplitudes $H_{yj}(z)$, $H_{zj}(z)$, and $E_{xj}(z)$ within each dielectric layer are written as $(a_j \exp(ikq_jz) + b_j \exp(-ikq_jz))$, where $q_j = \sqrt{\varepsilon_j\mu_j - \beta^2}$. Here j indicates layers A and B with electric permittivity ε_j and magnetic permeability μ_j, respectively. For an external medium (water), $q_s = -i\sqrt{\varepsilon_s\mu_s - \beta^2}$ [35,36]. Boundary conditions at the interfaces are defined based on the Maxwell equations [31]:

$$\begin{aligned} \hat{n}\times(\vec{H}_2 - \vec{H}_1) &= \sigma_g(\omega)\vec{E}, \\ \hat{n}\times(\vec{E}_2 - \vec{E}_1) &= 0. \end{aligned} \tag{2}$$

Here, $\hat{n}$ is the unit vector parallel to the z axis and $\sigma_g(\omega)$ is the optical conductivity of the graphene layer. Within the random phase approximation and without an external electromagnetic field, the optical conductivity of the graphene is given by the Kubo formula [37]:

$$\begin{aligned} \sigma_g(\omega) &= \sigma_g^{\text{intra}}(\omega) + \sigma_g^{\text{inter}}(\omega), \\ \sigma_g^{\text{intra}}(\omega) &= \frac{e^2}{4\hbar}\frac{i}{2\pi}\left\{\frac{16k_BT}{\hbar\omega}\ln\left(2\cosh\left(\frac{\mu_c}{2k_BT}\right)\right)\right\}, \\ \sigma_g^{\text{inter}}(\omega) &= \frac{e^2}{4\hbar}\left\{\frac{1}{2} + \frac{1}{\pi}\arctan\frac{\hbar\omega - 2\mu_c}{2k_BT}\right. \\ &\quad \left. - \frac{i}{2\pi}\ln\frac{(\hbar\omega + 2\mu_c)^2}{(\hbar\omega - 2\mu_c)^2 + (2k_BT)^2}\right\}, \end{aligned} \tag{3}$$

where e, k_B, μ_c, ω, and $\hbar = \frac{h}{2\pi}$ are electron charge, Boltzmann constant, temperature, chemical potential, angular frequency, and the reduced Plank's constant, respectively. μ_c can be controlled by applying a gate voltage. These expressions show that the interband contribution plays a significant role around the absorption threshold, $\hbar\omega \approx 2\mu_c$, while the intraband contribution is important at relatively low frequencies, $\hbar\omega < \mu_c$ [35,36]. By using the transfer matrix method [34,35], one can show that the field coefficients in the first layer of the jth and $(j+1)$th periods are related by the following equation:

$$\begin{pmatrix} a_{j+1} \\ b_{j+1} \end{pmatrix} = \begin{pmatrix} A & B \\ C & D \end{pmatrix}\begin{pmatrix} a_j \\ b_j \end{pmatrix}, \tag{4}$$

where A, B, C, and D for the TM polarization are given as

$$\begin{aligned} A &= \frac{1}{4}e^{ikq_ad_a}[(1 + t_1 - t_2)(1 + t_3 - t_4)e^{ikq_bd_b} \\ &\quad + (1 - t_1 + t_2)(1 - t_3 - t_4)e^{-ikq_bd_b}], \\ B &= \frac{1}{4}e^{ikq_a(d_a - 2d_t)}[(1 + t_1 - t_2)(1 + t_3 - t_4)e^{ikq_bd_b} \\ &\quad + (1 - t_1 + t_2)(1 - t_3 - t_4)e^{-ikq_bd_b}], \\ C &= \frac{-1}{4}e^{-ikq_a(d_a - 2d_t)}[(1 + t_1 - t_2)(1 - t_3 + t_4)e^{ikq_bd_b} \\ &\quad + (1 - t_1 + t_2)(1 + t_3 + t_4)e^{-ikq_bd_b}], \\ D &= \frac{-1}{4}e^{-ikq_ad_a}[(1 + t_1 - t_2)(1 - t_3 + t_4)e^{ikq_bd_b} \\ &\quad + (1 - t_1 + t_2)(1 + t_3 + t_4)e^{-ikq_bd_b}], \end{aligned} \tag{5}$$

with

$$t_1 = \frac{q_b \varepsilon_a}{q_a \varepsilon_b}, \qquad t_2 = \frac{\sigma k q_b}{\omega \varepsilon_0 \varepsilon_b}, \qquad t_3 = \frac{q_a \varepsilon_b}{q_b \varepsilon_a}, \qquad t_4 = \frac{\sigma k q_a}{\omega \varepsilon_0 \varepsilon_a}.$$

The eigenvalues of the matrix $\binom{A\ B}{C\ D}$, i.e., $(\lambda = \mathrm{Re}(A) \pm \sqrt{(\mathrm{Re}(A))^2 - 1})$ play important roles in the surface waves, which, for the TM polarization, are obtained from the following equations:

$$\frac{q_a \varepsilon_s}{q_s} + \frac{i\sigma q_a}{\omega \varepsilon_0} = i\varepsilon_a \frac{\lambda - A + B \exp(-2ikq_a d_s)}{\lambda - A - B \exp(-2ikq_a d_s)}. \tag{6}$$

The reflection of the structure is given by

$$r = \frac{M_{21}}{M_{11}}, \qquad R = |r|^2, \tag{7}$$

where M_{11} and M_{21} are the elements of the total transfer matrix that relate the field coefficients of the first layer to the ones of the last layer of the whole structure [31] as

$$\begin{pmatrix} a_{\text{prism}} \\ b_{\text{prism}} \end{pmatrix} = M \begin{pmatrix} a_{\text{water}} \\ b_{\text{water}} \end{pmatrix}. \tag{8}$$

3. NUMERICAL RESULTS AND DISCUSSION

In this work, we investigate a one-dimensional PhC biosensor of five periods consisting of the isotropic and non-magnetic alternate dielectric layers of TiO_2 and SiO_2 with the graphene nanolayers imbedded between the adjacent dielectric layers under the Kretschmann configuration (Fig. 1). There are a few graphene layers in the surface, which are denoted by N_{gs}. The refractive indices of the TiO_2 and SiO_2 layers are assumed to be $2.22 + i\gamma_{TiO_2}$ and $1.46 + i\gamma_{SiO_2}$, respectively, with thickness of 10 μm. The imaginary parts of the refractive indices refer to the losses in the dielectric layers. These losses include the intrinsic material absorption and the scattering losses in the incident light [16,23,38] ($\gamma_{SiO_2} = 0$ and $\gamma_{TiO_2} = 10^{-3}$, in this work). It is well known that the truncated PhCs can support BSW. For this purpose, we take the thickness of the termination layer as $d_c = \tau d_{TiO_2}$, with $\tau \in [0, 1]$ [39] ($\tau = 0.7$, in this work). We assume that our proposed structure is in contact with water, whose refractive index (n_s) changes from 1.33 (pure water) to 1.36 owing to the presence of analyte. Since the graphene is a material with low losses in the terahertz and far-IR frequencies [14], we limit our calculations to these regions. First, we compare the TM band structure of our proposed system with the band structure of a similar system without the graphene nanolayers (Fig. 2). The white and shaded areas show the forbidden and the passbands, respectively. As is obvious from the figures, unlike the structure without the graphene nanolayers, our structure has two forbidden bands in the given frequency region (0–8 THz). The lower forbidden band, which has been called the graphene induced bandgap (GIBG) [36], is due to the existing graphene nanolayers and the upper forbidden band is the conventional Bragg gap. To continue, we numerically solved Eq. (6) to obtain the dispersion of the surface modes as a function of β for different numbers of surface graphene layers N_{gs}. The surface modes are depicted by different curves at both the GIBG and the Bragg gap in Fig. 2(a). To compare the results, we plotted the dispersion of the surface modes of the conventional

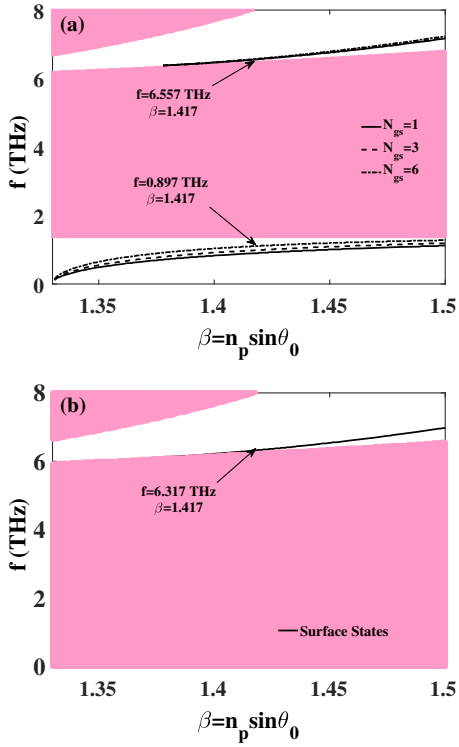

Fig. 2. Band structure and the dispersion of the surface modes (a) in the 1D-PhC containing graphene monolayers with different numbers of surface graphene layers N_{gs} and (b) in the 1D-PhC without the graphene monolayers as functions of β ($n_p = 1.515$).

structure without the graphene layers in Fig. 2(b). Since the optical conductivity of the surface graphene layers depends on the number of its layers as $\sigma' = N_g \sigma$ [30], Fig. 2(a), as we expect, shows that the dispersion of surface modes within the GIBG depends on the number of graphene layers at the surface of the biosensor, while the dispersion of the surface modes in the Bragg gap (Bloch surface modes) is nearly independent of the number of surface graphene layers N_{gs}. However, the thickness of the termination layer (d_c), the polarization, and the incident light frequency are other parameters that play significant roles in the dispersion of the Bloch surface waves, [40–42]. As one knows, the surface mode can be coupled to the incident light at a particular incident angle greater than the total internal reflection angle ($\theta_c = \sin^{-1}(n_s/n_p)$) and is observed as a sharp dip in the reflection spectrum. The depth and the width of this dip strongly depend on the dielectric losses and the refractive index of the sensing medium.

In the following discussion, in order to compare the performance of the graphene-based PhC biosensor with the conventional PhC biosensor, the reflection spectra of both structures are considered. In Fig. 3 we plotted the reflection of the structure at three different frequencies corresponding to the surface modes of Fig. 2 with the identical $\beta = 1.417$. Two modes belong to the graphene-based structure with $N_{gs} = 1$, and their reflection spectra are shown with the solid and dotted lines. The third mode belongs to the graphene-less structure, and its reflection is shown with the dashed line in Fig. 3. From the figure, it is apparent that the width of the dip at the refection

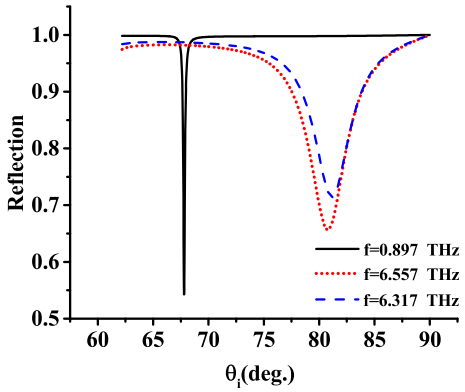

Fig. 3. Reflection spectra of the structure as functions of the incident angle θ_i correspond to the GIBG surface mode (solid line), the Bragg gap surface mode (dotted line) of the graphene-based structure, and the Bragg gap surface mode (dashed line) of the graphene-less structure.

spectrum that corresponds to the surface mode of the GIBG is narrower than those that correspond to the modes of the Bragg gaps of the structures with and without graphene nanolayers. For sensing purposes, we look for the surface modes with extended electric field profiles. In Fig. 4, the electric field profiles of the three modes corresponding to Fig. 3 are plotted as functions of the normal distance z. Because of the losses of the TiO_2 layers of the PhC, the EM wave has a decaying nature in the TiO_2 layers and a propagating nature in the SiO_2 layers of the structure. From Fig. 4, it is clear that the surface mode of the GIBG (solid line) is extended to the analyte side more than the surface modes of the Bragg gaps of the structure with (dotted line) or without (dashed line) the graphene nanolayers, which makes it useful for probing large volumes of aqueous solution. Moreover, the electric profile of the GIBG surface mode is localized more than those of the Bragg gap modes in the layered structure of the biosensor.

Figure 5 depicts the resonance angles in the reflection spectrum versus the refractive index of the sensing medium, which

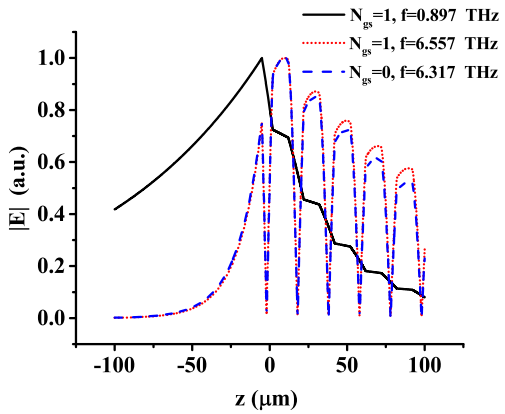

Fig. 4. Electric field profiles of the GIBG surface modes (solid line), the Bragg gap surface mode (dotted line) of the graphene-based structure, and the Bragg gap surface mode (dashed line) of the graphene-less structure.

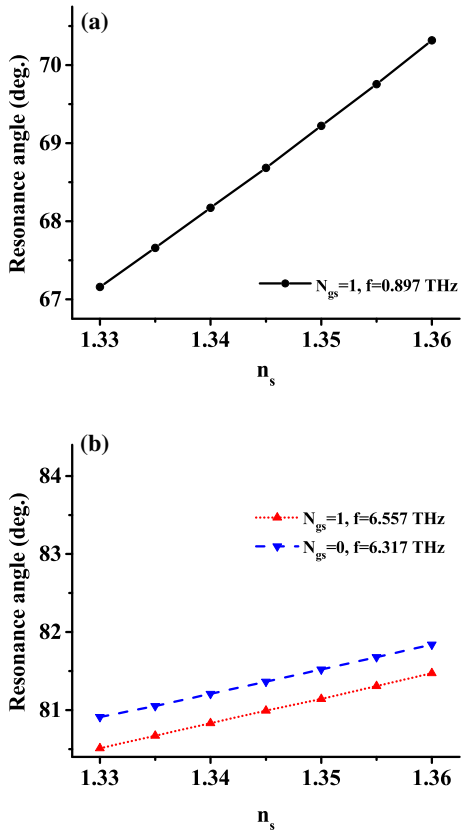

Fig. 5. Influence of the refractive index changes of the sensing medium on (a) the GIBG mode's resonance angle and (b) the Bragg mode's resonance angle.

changes from $n_s = 1.33$ (pure water) to $n_s = 1.36$. From the figure, one can see that the resonance angle is very sensitive to the refractive index of the sensing medium in the case of the GIBG mode. In contrast, the resonance angles in the reflection spectra of the structure corresponding to the Bragg gap surface modes are not highly sensitive to the change of n_s. To determine the angular sensitivity of the biosensor, one needs to calculate the slope of these diagrams, $S_\theta = \frac{\Delta\theta_{res}}{\Delta n_s}$ [27,38,42–45]. The angular sensitivities of the biosensor at two frequencies, $f = 0.897$ THz and $f = 6.557$ THz, are 117.042 and 35.638, respectively. In conventional 1D-PhCs, the sensitivity for $f = 6.317$ THz is 34.357, which is very close to those reported by Paeder *et al.* [42] and Li *et al.* [38].

To achieve a better perspective on the performance of the proposed one-dimensional graphene PhC (1D-GPhC) biosensor, the study of the full width at half-minimum (FWHM) of the resonance dip helps us to identify the exact resonance angle. The narrower FWHM becomes, the more detection accuracy is acquired. Detection accuracy can be defined as DA = 1/FWHM [43–45]. Figure 6 displays the detection accuracy of the selected surface modes in the 1D-GPhC and the 1D-PhC versus the refractive index of the sensing medium. From the figure, the trend is obviously downward in the case of the surface mode in GIBG with $f = 0.897$ THz. The detection accuracy of PBG modes in the structures with and without the graphene nanolayers, meanwhile, remain nearly constant.

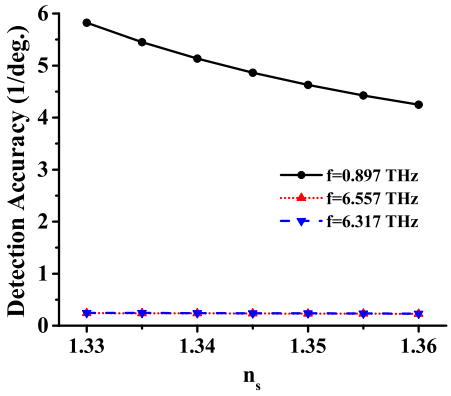

Fig. 6. Detection accuracy versus the refractive index of the sensing medium for the surface modes in the GIBG and the Bragg gap.

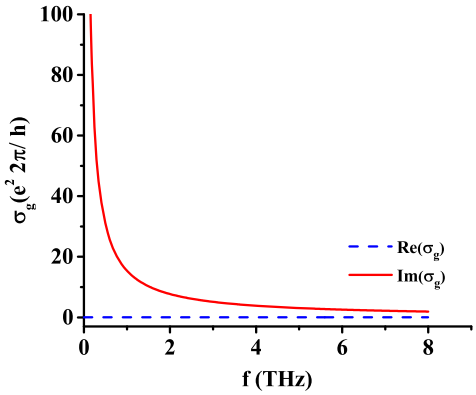

Fig. 7. Surface conductivity of the graphene as a function of frequency.

All behaviors described above have a simple explanation that can clarify them by the graphene surface conductivity [Eq. (3)]. As can be seen from Fig. 7, although $\mathrm{Im}(\sigma_g)$ substantially changes in the frequency interval of 0–4 THz, the trend of $\mathrm{Re}(\sigma_g)$ is steady and its quantity is almost zero. Therefore, $\mathrm{Im}(\sigma_g)$ plays an unrivaled role in the light–matter interaction properties of graphene, and its sign is particularly important, as well. While graphene layers with $\mathrm{Im}(\sigma_g) > 0$ support waves with TM polarization and behave like a very thin metal, those with $\mathrm{Im}(\sigma_g) < 0$ can weakly guide the wave with TE polarization [33].

From the numerical results obtained here, it is obvious that GIBG modes have great influence on sensing. Hence, it seems useful to study the optical sensing of the GIBG modes when the number of surface graphene layers varies from 1 to 6. From Fig. 8, one can see that, with increasing N_{gs}, the resonance dip shifts to greater angles. To further investigate the effect of surface graphene sheets on the performance of the described 1D-GPhC-biosensor, we introduce a figure of merit (FOM), which is defined as [16,44,45]

$$\mathrm{FOM} = \frac{S_\theta = \frac{\Delta\theta_{\mathrm{res}}}{\Delta n_s}}{\mathrm{FWHM}}(1 - \mathrm{MRR}), \tag{9}$$

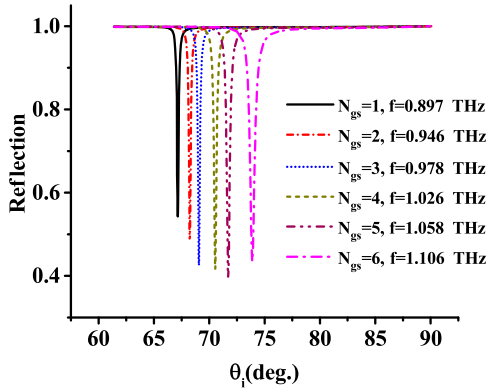

Fig. 8. Effect of the number of surface graphene layers on the reflection spectrum of the biosensor.

where MRR is the minimum reflectance at resonance. Table 1 indicates the FOM of the proposed biosensor when the number of graphene layers deposited on the surface varies from 1 to 6 with $\beta = 1.417$. The data in the first row belong to a 1D-PhC. It seems that the number of graphene layers on the surface has great impact on the performance of the 1D-GPhC biosensor. The results show that the angular sensitivity of the structure for the surface mode of the GIBG is enhanced by increasing the number of graphene layers ($\sigma' = N_{gs}\sigma$), which is in contrast to those of Bragg gaps.

To achieve a deeper understanding of the performance of the proposed biosensor, the biosensor phase behaviors are studied. Li *et al.* [26,38] have shown that the resonance dips in the reflection spectrum appear when the layers have losses ($\gamma \neq 0$). However, the step-like behavior of the phase around the resonance angle still remains large. Therefore, detection based on the phase differences is a powerful alternative approach to the reflectivity intensity detection for sensing. Phase (ϕ_p) is given by

$$r_p = |r_p| e^{-i\phi_p}, \tag{10}$$

in which r is calculated by Eq. (7). In this equation, p is related to TM polarization, and $\delta\phi = -\phi_p$ is the phase difference [14,26,38,46]. In Fig. 9(a) the phase shifts $\delta\phi$ over the incident

Table 1. Figures of Merit and Sensitivities for Two Selected Surface Modes with Various Surface Graphene Layers ($\beta = 1.417$)

Graphene Layer	f(THz)	$S_\theta = \frac{\Delta\theta_{\mathrm{res}}}{\Delta n_s}$	FOM
0 (1D-PhC)	6.317	34.357	2.204
1 (1D-GPhC)	0th gap = 0.897	117.042	283.081
	1st gap = 6.557	35.638	2.688
2	0th gap = 0.946	122.286	282.748
	1st gap = 6.557	35.546	2.765
3	0th gap = 0.978	126.901	327.282
	1st gap = 6.5825	35.500	2.859
4	0th gap = 1.026	135.755	262.320
	1st gap = 6.557	35.409	2.933
5	0th gap = 1.058	143.631	280.900
	1st gap = 6.557	35.363	3.025
6	0th gap = 1.106	161.917	169.152
	1st gap = 6.557	35.317	3.122

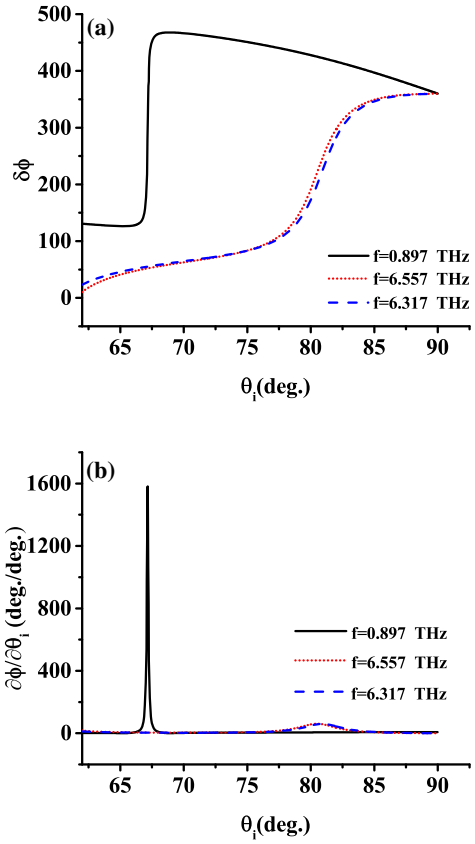

Fig. 9. (a) Phase differences and (b) plot of $\frac{\partial\delta\phi}{\partial\theta}$ versus the incident angle for the surface modes in the structures with and without graphene nanolayers shown in Fig. 2.

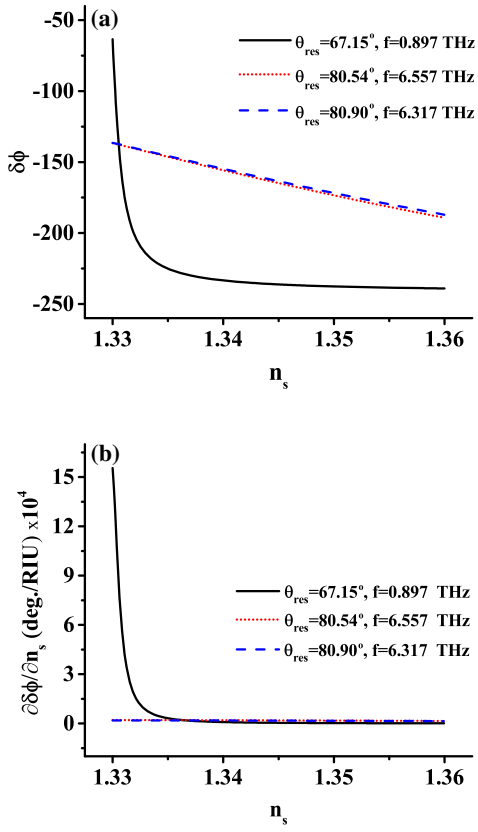

Fig. 10. (a) Phase differences and (b) the plot of $\frac{\partial\delta\phi}{\partial n_s}$ versus the sensing medium refractive index for the surface modes in the structures with and without graphene nanolayers shown in Fig. 2.

angle are plotted for the SWs displayed in Fig. 2. One can see from the figure that although the phase shifts are step-like around resonance angles, $\delta\phi$ experiences drastic change around $\theta_{\text{res}} = 67.15°$ in the case of a GIBG mode with $f = 0.897$ THz. To demonstrate this more clearly, the function $\partial\delta\phi/\partial\theta$ versus incident angle is shown in Fig. 9(b). From this figure, we see that, for the GIBG mode, $\partial\delta\phi/\partial\theta$ has its peak value of 1600 in the resonance angle 67.15°, while for the Bloch modes, their pick values reach to almost 60 at their resonance angles of 80.54° and 80.90° in the structures with and without graphene nanolayers, respectively.

Figure 10(a) shows the effect of small changes in the refractive index of the sensing medium (n_s) on the phase differences. As can be seen, $\delta\phi$ is very sensitive to change of the refractive index in the case of the GIBG mode in comparison with the Bloch modes with $f = 6.557$ THz and $f = 6.317$ THz in the structures with and without graphene nanolayers, respectively. To show this more clearly, the function $S_\phi = \partial\delta\phi/\partial n_s$ (phase sensitivity) [14,38,46] versus the refractive index of the sensing medium is plotted in Fig. 10(b). As the figure reveals, the phase sensitivity of the GIBG mode is 10^4 times higher than those of the Bloch modes in both structures. Furthermore, as our results show, the phase sensitivity is higher than the angular sensitivity.

Finally, it seems useful to study the phase sensitivity $\partial\delta\phi/\partial n_{\text{bio}}$ over surface refractive index changes (n_{bio}). Here, the thickness of the biolayer is $d_{\text{bio}} = 10$ nm. From Fig. 11, it is obvious that, by comparison with Fig. 10(b), the phase sensitivity for the selected modes is significantly reduced. This behavior is stronger for the GIBG mode. It is a predictable result and can be obtained from Fig. 4. It seems the large evanescent tail of the GIBG mode can be useful for probing large volumes of water.

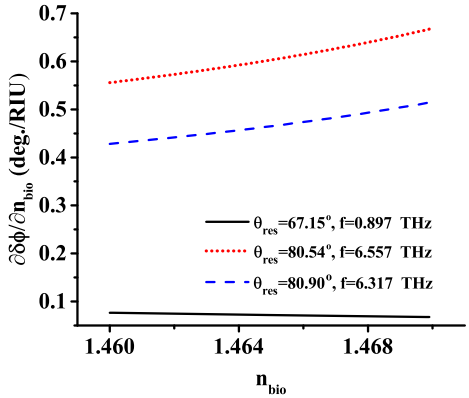

Fig. 11. Plot of $\frac{\partial\delta\phi}{\partial n_{\text{bio}}}$ versus the surface refractive index changes (n_{bio}) for the surface modes in the structures with and without graphene nanolayers shown in Fig. 2.

4. CONCLUSION

In this study, we used the transfer matrix method for comparing the performance of two similar photonic crystal biosensors: one includes graphene nanolayers and the other one is a conventional PhC. Our theoretical results illustrated that introducing graphene nanolayers at the interface between two adjacent dielectric layers not only changes the band structure and adds an additional forbidden band, but it has significant influence on the resonance dip in the reflection spectrum, as well. Furthermore, we studied the role of the surface graphene layers in the efficiency of a one-dimensional graphene PhC biosensor. The investigations showed that the increase of graphene layers on the surface of a 1D-GPhC enhance the adsorption, which results in higher sensitivity. In addition, we calculated the phase related to p polarization. Results showed that the phase difference of the surface mode in a GIBG is very sensitive to the refractive index changes in the analyte side of the biosensor and the incident angle. Moreover, we compared the phase sensitivity with the angular sensitivity, which is calculated by the slope of the resonance angle over the sensing medium's refractive index range. Results demonstrated that the phase sensitivity is higher than the angular sensitivity. Thus, it can be a great choice for investigating the performance of our biosensor with more accuracy. Finally, we calculated the phase sensitivity over surface refractive index changes (n_{bio}). Results showed that the phase sensitivities for the selected modes are considerably declined in contrast to those of bulky refractive index changes of the external medium (n_s). Studies illustrated that the proposed biosensor might be useful for sensing analytes in large volumes of aqueous solution.

REFERENCES

1. J. D. Joannopoulos, R. D. Meade, and J. N. Winn, *Photonic Crystals: Molding the Flow of Light* (Princeton University, 1995).
2. K. Sakoda, *Optical Properties of Photonic Crystals*, Vol. **80** of Springer Series in Optical Sciences (Springer, 2004).
3. Q. Gong and X. Hu, *Photonic Crystals: Principles and Applications* (CRC Press, 2014).
4. K. Inoue and K. Ohtaka, *Photonic Crystals: Physics, Fabrication and Applications* (Springer, 2013).
5. J. Polo, T. Mackay, and A. Lakhtakia, *Electromagnetic Surface Waves: A Modern Perspective* (Newnes, 2013).
6. D. Smirnova, P. Buslaev, I. Iorsh, I. V. Shadrivov, P. A. Belov, and Y. S. Kivshar, "Deeply subwavelength electromagnetic Tamm states in graphene metamaterials," Phys. Rev. B **89**, 245414 (2014).
7. P. Yeh, A. Yariv, and A. Cho, "Optical surface waves in periodic layered media," Appl. Phys. Lett. **32**, 104–105 (1978).
8. A. P. Vinogradov, A. V. Dorofeenko, A. M. Merzlikin, and A. A. Lisyansky, "Surface states in photonic crystals," Phys. Usp. **53**, 243–256 (2010).
9. A. Namdar, I. V. Shadrivov, and Y. S. Kivshar, "Backward Tamm states in left-handed metamaterials," Appl. Phys. Lett. **89**, 114104 (2006).
10. J. Barvestani, M. Kalafi, and A. Soltani-Vala, "Surface optical waves in semi-infinite one-dimensional photonic crystals containing alternating layers of positive and negative media with a cap layer," Acta Phys. Pol. A **112**, 1089–1094 (2007).
11. M.-I. Baraton, *Sensors for Environment, Health and Security: Advanced Materials and Technologies* (Springer, 2008).
12. M. J. Serpe, Y. Kang, and Q. M. Zhang, *Photonic Materials for Sensing, Biosensing and Display Devices* (Springer, 2016).
13. V. N. Konopsky and E. V. Alieva, "Photonic crystal surface waves for optical biosensors," Anal. Chem. **79**, 4729–4735 (2007).
14. K. V. Sreekanth, S. Zeng, K.-T. Yong, and T. Yu, "Sensitivity enhanced biosensor using graphene-based one-dimensional photonic crystal," Sens. Actuators B **182**, 424–428 (2013).
15. K. V. Sreekanth, S. Zeng, J. Shang, K.-T. Yong, and T. Yu, "Excitation of surface electromagnetic waves in a graphene-based Bragg grating," Sci. Rep. **2**, 737 (2012).
16. A. Sinibaldi, R. Rizzo, G. Figliozzi, E. Descrovi, N. Danz, P. Munzert, A. Anopchenko, and F. Michelotti, "A full ellipsometric approach to optical sensing with Bloch surface waves on photonic crystals," Opt. Express **21**, 23331–23344 (2013).
17. M. Liscidini and J. Sipe, "Enhancement of diffraction for biosensing applications via Bloch surface waves," Appl. Phys. Lett. **91**, 253125 (2007).
18. F. Frascella, C. Petri, S. Ricciardi, L. Napione, P. Munzert, U. Jonas, J. Dostalek, F. Bussolino, C. Pirri, and E. Descrovi, "Hydrogel-terminated photonic crystal for label-free detection of angiopoietin-1," J. Lightwave Technol. **34**, 3641–3645 (2015).
19. F. Frascella, S. Ricciardi, P. Rivolo, V. Moi, F. Giorgis, E. Descrovi, F. Michelotti, P. Munzert, N. Danz, L. Napione, M. Alvaro, and F. Bussolino, "A fluorescent one-dimensional photonic crystal for label-free biosensing based on Bloch surface waves," Sensors **13**, 2011–2022 (2013).
20. F. Michelotti, B. Sciacca, L. Dominici, M. Quaglio, E. Descrovi, F. Giorgis, and F. Geobaldo, "Fast optical vapour sensing by Bloch surface waves on porous silicon membranes," Phys. Chem. Chem. Phys. **12**, 502–506 (2010).
21. A. Sinibaldi, A. Anopchenko, R. Rizzo, F. Michelotti, N. Danz, P. Munzert, P. Rivolo, S. Ricciardi, and F. Frascella, "Phase-sensitive Bloch surface wave biosensors," in *AISEM Annual Conference, XVIII* (IEEE, 2015).
22. F. Michelotti and E. Descrovi, "Temperature stability of loch surface wave biosensors," Appl. Phys. Lett. **99**, 231107 (2011).
23. M. Shinn and W. Robertson, "Surface plasmon-like sensor based on surface electromagnetic waves in a photonic band-gap material," Sens. Actuators B **105**, 360–364 (2005).
24. S. H. Choi and K. M. Byun, "Investigation on an application of silver substrates for sensitive surface plasmon resonance imaging detection," J. Opt. Soc. Am. A **27**, 2229–2236 (2010).
25. A. Shalabney and I. Abdulhalim, "Electromagnetic fields distribution in multilayer thin film structures and the origin of sensitivity enhancement in surface plasmon resonance sensors," Sens. Actuators A **159**, 24–32 (2010).
26. Y. Li, T. Yang, S. Song, Z. Pang, G. Du, and S. Han, "Phase properties of Bloch surface waves and their sensing applications," Appl. Phys. Lett. **103**, 041116 (2013).
27. L. Wu, H. Chu, W. Koh, and E. Li, "Highly sensitive graphene biosensors based on surface plasmon resonance," Opt. Express **18**, 14395–14400 (2010).
28. X. Fan, I. M. White, S. I. Shopova, H. Zhu, J. D. Suter, and Y. Sun, "Sensitive optical biosensors for unlabeled targets: a review," Anal. Chim. Acta **620**, 8–26 (2008).
29. Y. V. Bludov, N. M. Peres, and M. I. Vasilevskiy, "Unusual reflection of electromagnetic radiation from a stack of graphene layers at oblique incidence," J. Opt. **15**, 114004 (2013).
30. Y. Xiang, J. Guo, X. Dai, S. Wen, and D. Tang, "Engineered surface Bloch waves in graphene-based hyperbolic metamaterials," Opt. Express **22**, 3054–3062 (2014).
31. T. Zhan, X. Shi, Y. Dai, X. Liu, and J. Zi, "Transfer matrix method for optics in graphene layers," J. Phys. **25**, 215301 (2013).
32. G. W. Hanson, "Quasi-transverse electromagnetic modes supported by a graphene parallel-plate waveguide," J. Appl. Phys. **104**, 084314 (2008).
33. G. W. Hanson, A. B. Yakovlev, and A. Mafi, "Excitation of discrete and continuous spectrum for a surface conductivity model of graphene," J. Appl. Phys. **110**, 114305 (2011).
34. P. Yeh, A. Yariv, and C.-S. Hong, "Electromagnetic propagation in periodic stratified media, I: general theory," J. Opt. Soc. Am. **67**, 423–438 (1977).
35. J. Martorell, D. Sprung, and G. Morozov, "Surface TE waves on 1D photonic crystals," J. Opt. A **8**, 630–638 (2006).
36. A. Madani and S. R. Entezar, "Optical properties of one-dimensional photonic crystals containing graphene sheets," Phys. B Condens. Matter **431**, 1–5 (2013).

37. L. Falkovsky and S. Pershoguba, "Optical far-infrared properties of a graphene monolayer and multilayer," Phys. Rev. B **76**, 153410 (2007).
38. Y. Li, T. Yang, Z. Pang, G. Du, S. Song, and S. Han, "Phase-sensitive Bloch surface wave sensor based on variable angle spectroscopic ellipsometry," Opt. Express **22**, 21403–21410 (2014).
39. F. Villa, L. Regalado, F. Ramos-Mendieta, J. Gaspar-Armenta, and T. Lopez-Ríos, "Photonic crystal sensor based on surface waves for thin-film characterization," Opt. Lett. **27**, 646–648 (2002).
40. M. Kalafi, A. Soltani-Vala, and J. Barvestani, "Surface optical waves in semi-infinite one-dimensional photonic crystals with a thin nonlinear cap layer," Opt. Commun. **272**, 403–406 (2007).
41. M. Liscidini and J. Sipe, "Analysis of Bloch-surface-wave assisted diffraction-based biosensors," J. Opt. Soc. Am. B **26**, 279–289 (2009).
42. V. Paeder, V. Musi, L. Hvozdara, S. Herminjard, and H. Herzig, "Detection of protein aggregation with a Bloch surface wave based sensor," Sens. Actuators B **157**, 260–264 (2011).
43. P. K. Maharana and R. Jha, "Chalcogenide prism and graphene multilayer based surface plasmon resonance affinity biosensor for high performance," Sens. Actuators B **169**, 161–166 (2012).
44. M. Tahmasebpour, M. Bahrami, and A. Asgari, "Design study of nanograting-based surface plasmon resonance biosensor in the near-infrared wavelength," Appl. Opt. **53**, 1449–1458 (2014).
45. W. K. Jung, N.-H. Kim, and K. M. Byun, "Numerical study on an application of subwavelength dielectric gratings for high-sensitivity plasmonic detection," Appl. Opt. **51**, 4722–4729 (2012).
46. S. R. Entezar, "Effect of surface plasmon polaritons on the sensitivity of refractive index measurement using total internal reflection method," J. Magn. Magn. Mater. **381**, 203–207 (2015).